

Combinatorial Discovery of Irradiation Damage Tolerant Nano-structured W-based alloys

Haechan Jo ^a, Sanghun Park ^a, Daegun You ^a, Sooran Kim ^b, Dongwoo Lee ^{a, *}

^a School of Mechanical Engineering, Sungkyunkwan University (SKKU), Suwon 16419, Republic of Korea

^bDepartment of Physics Education, Kyungpook National University (KNU), Daegu 41944, Republic of Korea

*Corresponding Authors Email: dongwoolee@skku.edu

Abstract

One of the challenges in fusion reactors is the discovery of plasma facing materials capable of withstanding extreme conditions, such as radiation damage and high heat flux. Development of fusion materials can be a daunting task since vast combinations of microstructures and compositions need to be explored, each of which requires trial-and-error based irradiation experiments and materials characterizations. Here, we utilize combinatorial experiments that allow rapid and systematic characterizations of composition-microstructure dependent irradiation damage behaviors of nanostructured tungsten alloys. The combinatorial materials library of W-Re-Ta alloys was synthesized, followed by the high-throughput experiments for probing irradiation damages to the mechanical, thermal, and structural properties of the alloys. This highly efficient technique allows rapid identification of composition ranges with excellent damage tolerance. We find that the distribution of implanted He clusters can be significantly altered by the addition of Ta and Re, which play a critical role in determining property changes upon irradiation.

Keywords

Plasma-facing materials, Combinatorial synthesis, Nanocrystalline W-based alloys, High-throughput experiments, Helium-ion irradiation

1. Introduction

One of the technological challenges of commercialization of fusion reactors from a materials perspective is the development of suitable plasma facing materials (PFMs) that can withstand severe environments, such as irradiation damages and huge heat flux [1]. It is therefore required to investigate composition-microstructure dependent irradiation damages of PFM candidates. One of the most promising PFMs in a fusion reactor is tungsten because of its high melting point (3680 K), high thermal conductivity ($173 \text{ W} \cdot \text{m}^{-1} \cdot \text{K}^{-1}$) [2], low sputtering yield [3], low tritium retention [4], high heat load resistance [5], and high-temperature strength [6]. However, PFMs are adversely affected by the irradiation of the energetic neutrons and ions, which creates microstructural

defects [7]. Typical microstructural features of neutron-irradiated W are the formation of dislocation loops, voids, and irradiation-induced precipitates [8]. For hydrogen irradiation, supersaturation of hydrogen leads to blistering in the near-surface region. This phenomenon occurs even at a low irradiation energy range [9]. Moreover, implanted helium (He) ions are readily trapped by irradiation-induced defects, such as vacancies, dislocation loops, and voids resulting in the formation of He-bubbles [10], blisters [11], and even fuzzes [12]. These irradiation-induced defects and morphology changes cause severe degradation of W, leading to increased tritium retention [13], a high erosion rate [14], and decreased heat transfer capacity.

Previous studies have shown that irradiation damages can be mitigated by alloying with small amounts of additives to W. For example, W-Ta alloys not only exhibit higher ultimate tensile strength (UTS) and prevent crack propagation [15], but also suppress the formation of He bubbles [16], and fuzzes [17]. W-Re alloys are known to improve ductility [18], and effectively suppress defects formed by neutron irradiation [19]. Meanwhile, recent studies have revealed that nanostructured tungsten and its alloys and composites, which contain a high grain boundary (GB) density, are irradiation damage tolerant since GBs serve as effective trapping sites for irradiation-induced defects [20-22]. For instance, He-ion irradiated nanochannel W films effectively release He atoms to GBs, resulting in a lower areal density of He bubbles [23-25]. Similarly, S Si et al. reported that W-graphene nanostructured multilayers exhibit excellent radiation tolerance as the inserted graphene layers create new interfaces that act as effective sinks for He-induced defects [26]. O EI-Atwani et al. reported nanocrystalline W-based refractory high entropy alloys (HEAs) with outstanding radiation resistance under Kr-ion irradiation [27]. The W-based HEAs did not contain irradiation-induced dislocation loops and had negligible irradiation hardening. Processing techniques have been developed to fabricate the ultra-fine grained W at large scales [28] and deposition techniques were suggested to produce nanostructured coatings for PFMs [29, 30]

Although nanostructured W-alloys seem promising as PFMs, limited combinations of composition-microstructure have been explored. Irradiation damages of vast combinations of composition and microstructure need to be investigated in order to deepen our understanding on the irradiation damage tolerant materials and to discover novel alloys with the ideal set of properties. Trial-and-error based conventional irradiation experiments followed by materials characterizations, however, are inefficient to investigate the huge design space. In this work, combinatorial synthesis of nanostructured W-Ta, W-Re, and W-Re-Ta thin films was carried out to produce specimens with composition spreads. We then employed combinatorial and high-throughput experiments (HTEs) to investigate irradiation damages of the materials library [31-34]. The irradiation damage behaviors with respect to composition and microstructure were characterized by mechanical, thermal, and structural properties of the combinatorial samples. We demonstrate from this highly efficient technique that composition-microstructure combinations with the least irradiation damages can readily be discovered.

2. Experimental

2.1 Combinatorial film preparation

The nanocrystalline W-based alloys were magnetron sputter deposited on a 475 μm thick Si (100) wafer capped with a 200 nm thick LPCVD Si_3N_4 layer. The substrate was cut into a 20 mm \times 20 mm in-plane size for the W-Re-Ta systems and into a 20 mm \times 10 mm size for the W-Re and W-Ta systems. The sputter depositions were carried out without a substrate rotation to synthesize thin films with in-plane composition gradients [32]. The sputter guns and the substrate are tetragonally arranged such that different positions of the substrate have different relative fluxes of the vapors from each target. The pure W film was also deposited without a substrate rotation to induce a similar nanocolumnar structure to the alloy systems. For the sputter deposition process, the DC gun powers were set to 70 W, 20 W, and 30 W for W, Re, and Ta targets, respectively, to prepare for the alloy specimens. A gun power of 100 W was used for the pure W film. The depositions were carried out at a substrate temperature of 500 °C, and the Ar pressure and the base pressure of the vacuum chamber were 5×10^{-3} Torr and 2×10^{-7} Torr, respectively. Before all the deposition processes, a 10 nm thick Ti adhesion layer was deposited (DC power: 100 W, substrate rotation speed: 10 rpm, substrate temperature: 500 °C, Ar and base pressures: 5×10^{-3} and 2×10^{-7} Torr).

2.2 Film characterizations

The in-plane chemical composition gradient of the combinatorial films was determined using an Energy-dispersive X-ray Spectroscopy (EDS) in a Field Emission Scanning Electron Microscope (FESEM, JSM-7600F, JEOL). The spot size used was 1 $\mu\text{m} \times 1 \mu\text{m}$ and the accelerating voltage was set to 15 keV. The film thickness values of the combinatorial samples were measured to be $1.0 \pm 0.2 \mu\text{m}$ using a profilometer (DXT-A, Bruker) and confirmed with the cross-sectional TEM and SEM micrographs.

X-ray diffraction (XRD) measurements were performed in the Bragg-Brentano geometry (D8 advanced eco, Bruker). The film lattice parameter and FWHM were determined using the (110) peak. The lattice parameter was calculated through the d-spacing value using Bragg's law. For the crystallinity analysis, the FWHM value of the gaussian-fitted peak was measured. The cross-sectional transmission electron microscope (JEM-2100F, JEOL) images were taken for both un-irradiated and irradiated samples (at 200 keV). The 50 ~ 70 nm thick TEM samples were prepared by using a focused ion beam milling (3D FEG, Quanta) [35-37] with 30 kV Ga-ions (7 nA ~ 50pA). Before the milling process, a protective layer of Pt was deposited to prevent ion damages.

The electronic thermal conductivity (the electronic contribution of the thermal conductivity) was determined by the Wiedemann-Franz (W-F) law using electrical resistivity, which was measured by a custom-built 4-point measurement. A 4-point probe was configured in a line array with 1 mm of a spacing. The film electrical resistance (R) was determined using a current input of 1 mA through

a digital multimeter (3058e, RIGOL). Electrical resistance (R) was converted to resistivity (ρ) using film thickness (t) and a correction factor ($F = 4.23 \sim 4.36$) [38, 39] :

$$\rho = FRt. \quad (1)$$

The electronic thermal conductivity (κ_e) was calculated through the W-F law [40]:

$$\frac{\kappa_e}{\sigma} = LT, \quad (2)$$

where σ is electrical conductivity ($1/\rho$), L is the Lorenz number ($2.44 \times 10^{-8} W\Omega K^{-2}$), and T is the absolute temperature. The thermal conductivity determined by this method does not consider the thermal transport by phonons, which constitutes approximately 10 % of the total thermal conductivity for metals and alloys [40-42].

The hardness maps were determined by nanoindentation (KLA iNano) in the continuous stiffness measurement (CSM) mode and with a diamond Berkovich tip. Before running the experiments, a standard tip calibration was performed using a fused silica sample. The target load and strain rate used were 50 mN and 0.2 s^{-1} , respectively. The nanoindentation hardness values versus depth were determined using the Oliver & Pharr method [43]. We took the values at a 10% depth of the film thickness to avoid the substrate effect [44, 45]. A total of 16 positions per composition were analyzed (4×4 array, $25 \mu\text{m}$ intervals). The combinatorial synthesis method used in this work resulted in surface roughness of 20 nm, approximately. The measured hardness would be slightly underestimated by the sample roughness (Fig. S1), but would be slightly overestimated by the compressive residual stresses of the thin film.

2.3 First-principles calculations

First-principles calculations based on density function theory (DFT) were performed through the Vienna Ab initio simulation package (VASP). The generalized gradient approximation of Perdew-Burke-Ernzerhof has been implemented. Host atom valence states were treated using -W, Re, and Ta with PAW-PBE W_pv, Re_pv, Ta_pv, and the interstitial impurity atom – He with PAW-PBE He. The energy cutoff of 520 eV and a $5 \times 5 \times 5$ mesh of Monkhorst-pack points for the Brillouin zone integration were employed for the calculation.

3. Results

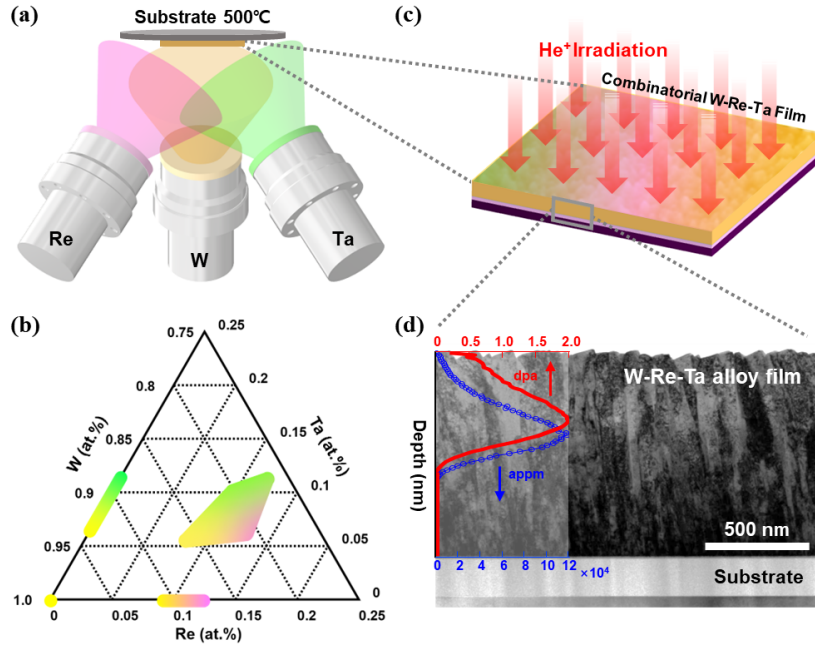


Fig. 1. (a) A schematic diagram of the combinatorial synthesis processing using magnetron sputtering for the nanostructured binary and ternary alloys with W, Re, and Ta. (b) Composition ranges of the nanostructured alloys investigated in this work. (c) An illustration of the He-ion irradiation experiment conducted on the combinatorial specimen. (d) A cross-sectional TEM image of a W-Re-Ta alloy film. Displacement per atom (dpa) and He⁺ ion concentration versus depth calculated by SRIM 2013 are shown.

Pure W and binary (W-Re and W-Ta), ternary (W-Re-Ta) nanostructured alloys with composition spreads were prepared by a magnetron co-sputter deposition process with a substrate temperature of 500 °C, as schematically illustrated in Fig. 1(a). During the deposition, the substrate was not rotated, producing 1 μm thick thin film specimens with in-plane chemical composition gradients. The composition ranges investigated in this work is shown in Fig. 1(b), which were determined by energy dispersive X-ray spectroscopy (EDS): pure W, W₈₇₋₉₁Re₉₋₁₃, W₈₈₋₉₄Ta₆₋₁₂, and W₇₅₋₈₇Re₈₋₁₃Ta₅₋₁₂ ranges were synthesized, which correspond to 50 distinct compositions with a 1 at. % spacing. Two specimens for each system under the same deposition condition were prepared, one of which was subjected to the mechanical, electrical, and microstructure characterizations in the un-irradiated state. The other specimen was used for the He-ion irradiation experiment, followed by the identical materials characterizations.

All the combinatorial specimens prepared in this work can be located within a 40 mm × 40 mm area together, where a uniform irradiation condition can be assured by the He-ion irradiation source (KOMAC, Korea Multi-Purpose

Accelerator Complex). He-ions with an energy of 200 keV and the fluence and flux of 2×10^{17} ions \cdot cm $^{-2}$ and 1.1×10^{13} ions \cdot cm $^{-2}$ s $^{-1}$, respectively were irradiated to the specimens in the growth direction of the films (see Fig. 1(c)). The irradiation experiment was performed in a vacuum chamber ($\sim 1.0 \times 10^{-5}$ Torr) at room temperature. The damage profile calculated by Stopping and Range of Ions in Matter 2013 (SRIM 2013) using the experimental irradiation conditions employed and with the displacement threshold energy of 90 eV [46, 47] is shown in Fig. 1(d), together with a cross-sectional transmission electron microscopy (TEM) image of a W-Ta-Re nanostructured alloy. The damage profile shows a maximum of 2 dpa (displacement per atom) and 12 at. % He concentration at a depth of ~ 380 nm. Low homologous temperatures (the ratio of the deposition temperature to the melting point of the specimen) of the thin films resulted in a densely packed columnar nanostructure, which is consistent with the T-zone microstructure of the structure-zone model [48]. The nanocolumnar structure is expected to exhibit high damage tolerance as high-density grain boundaries can act as sinks for irradiation byproducts [49-52].

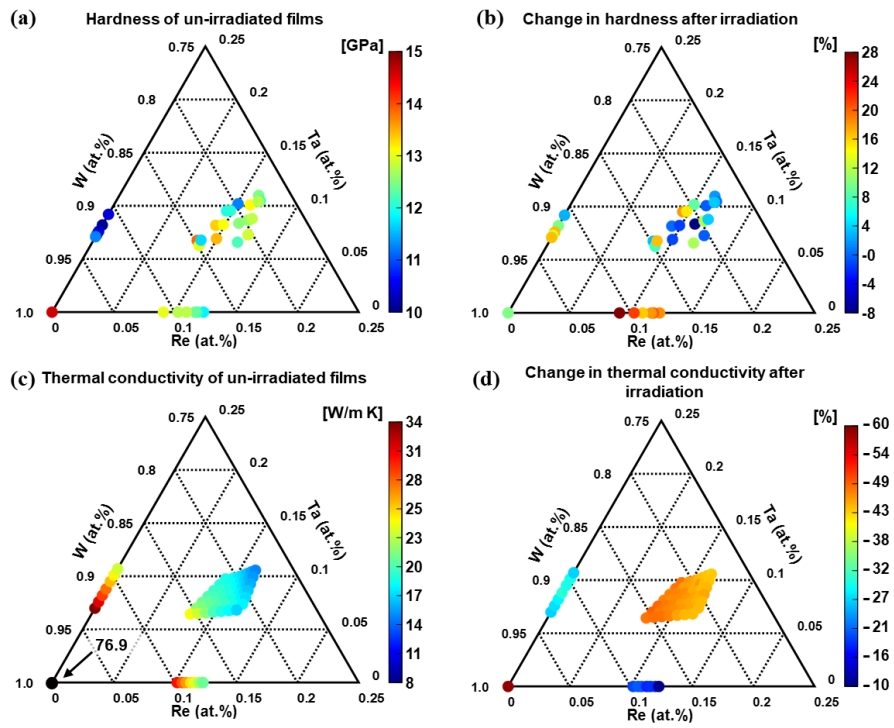


Fig. 2. (a) Hardness map of the un-irradiated combinatorial films. (b) The change in hardness of the specimens after He-ion irradiation. (c) Thermal conductivity map of the un-irradiated films. (d) The change in thermal conductivity after irradiation.

The irradiation-induced hardening of PFMs is one of the major degradation

mechanisms, which is closely related to the reliability of fusion reactors. We used nanoindentation to investigate composition-dependent degradation in the mechanical property of the combinatorial nanostructured alloys. As shown in Fig. 2(a), the nanoindentation hardness values of the un-irradiated alloy thin films of the W-Ta (10.1 ~ 10.5 GPa) and W-Re (11.8 ~ 13.0 GPa) are lower than the hardness of the pure W (14.6 GPa). It has been reported that Re solutes in W enhance the mobility of screw dislocations, resulting in solid solution softening [53-55]. On the other hand, Ta solutes in W generally increase hardness due to grain refinement and relative density improvement during bulk processing [56, 57]. As will be discussed later, the W-Ta system in this work has a relatively large grain size than the other systems, resulting in lower hardness values in our experiment [58].

Irradiation-induced hardening have been characterized by comparing the hardness maps acquired before and after He-ion irradiation (Fig. S2). As seen in Fig. 2(b), the change in hardness is more severe in the W-Re system (18 ~ 28 %), than in the pure W (9.8 %), W-Re-Ta (-8 ~ 18 %), and W-Ta (2.8 ~ 17 %) films. It is noticeable from the result that the composition ranges with small hardness changes are readily identifiable. For instance, the $W_{91}Ta_9$ and $W_{76-83}Re_{10-13}Ta_{7-11}$ composition regions have irradiation hardening rates below 4.9 %, which is half of the value of pure W (9.8 %).

A similar irradiation damage map can be acquired for the thermal property of the combinatorial thin film library. Fig. 2(c) shows the electronic thermal conductivity (κ_e) map of the un-irradiated combinatorial films, which was determined using the electrical resistivity map and through the Wiedemann-Franz (W-F) law (Fig. S3). The pure W film has the largest value of κ_e (76.9 W/m · K) and increment of solute concentration decreases κ_e as the solutes scatter the electron flow [56, 59]. Ta lowers κ_e more effectively than Re: $W_{90}Ta_{10}$ has 23.9 W/m·K, while $W_{90}Re_{10}$ has 29.5 W/m·K for κ_e . The result is somewhat unexpected because the grain size of the W-Ta system is larger than the W-Re alloys and bulk Ta (14.6 $\mu\Omega \cdot cm$ at 20 °C) has lower resistivity than bulk Re (22.2 $\mu\Omega \cdot cm$ at 20 °C) [60]. We attribute lower thermal conductivity in the W-Ta system than in the W-Re system to the larger degrees of the lattice distortion in W-Ta [61], as will be confirmed later. Since the W-Re-Ta films have higher overall solute concentrations than the binary films, they have lower electronic thermal conductivity.

After He-ion irradiation, κ_e was reduced for all the systems (see Fig. 2(d)) due to enhanced scattering of electron flow due to the irradiation-induced defects in the GBs and GIs (grain interiors). Reduction in κ_e is larger in the pure W film (- 60 %) than in the alloys with Re and/or Ta solutes, indicating that the solutes make the alloys more irradiation damage tolerant. Interestingly, the W-Re system that has the most severe mechanical irradiation damage showed the least degradation in κ_e among the investigated systems. As will be discussed later, this result is due to different distributions of He-irradiation induced defects in the W-Ta and W-Re systems. Composition ranges with small irradiation damages in κ_e

can effectively be identified in Fig. 2(d): changes in κ_e of $W_{89-93}Ta_{7-11}$ and $W_{87-90}Re_{10-13}$ are less than half of the thermal degradation in pure W (-60%).

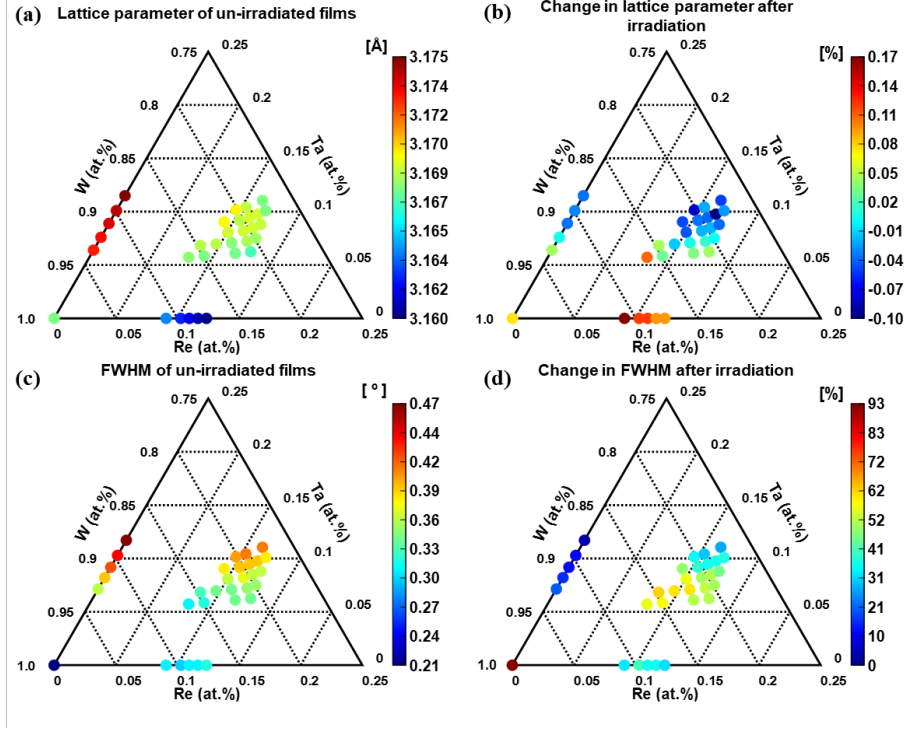


Fig. 3. XRD results of the combinatorial nanostructured thin films. The maps of (a) the lattice parameter of the un-irradiated films and (b) the change in the lattice parameter due to He irradiation. (c) The map of the FWHM from the (110) XRD peaks of the un-irradiated films and (d) the change in the FWHM due to He irradiation.

Microstructural analyses were carried out through a wafer scanning X-ray diffraction (XRD) technique for the un-irradiated and irradiated combinatorial thin film alloys (Fig. 3). We find that all the compositions of the W-alloys studied in this work formed a BCC phase (space group: $Im\bar{3}m$) with a (110) preferred orientation (Fig. S4). The lattice parameters of the un-irradiated combinatorial films are presented in Fig. 3(a). In the binary systems, increase in solute concentration in the W-Ta system leads to larger lattice parameters, while a reverse trend is found in the W-Re system. This trend is attributed to the relative atomic sizes of the solutes as compared with W: the radius of Ta (1.47 Å) is largest, followed by W (1.41 Å) and Re (1.38 Å) [62]. The combined effects of Ta (increasing lattice parameter) and Re (decreasing lattice parameter) can be seen for the W-Ta-Re ternary system.

The changes in the lattice parameters of the combinatorial thin films after He-

ion irradiation are presented in Fig. 3(b). The lattice parameter map of the irradiated films can be found in Fig. S5(a). The composition ranges with low irradiation damages in lattice parameter can be readily identified using Fig. 3(b): changes in the lattice parameter of $W_{89-92}Ta_{8-12}$ and $W_{77-84}Re_{9-12}Ta_{7-11}$ are less than half of the lattice swelling in pure W. He-ion implantation resulted in lattice swelling of the pure W (0.07 %) and the W-Re films (0.10 ~ 0.17 %). Smaller lattice swelling or even shrinkage is observed in the W-Ta and W-Re-Ta systems after irradiation (- 0.10 % ~ 0.11%). There are two competing mechanisms that are responsible for the different degrees of lattice swelling. First, lattice shrinkage can occur by the irradiation-induced relaxation of the non-equilibrium crystal structure that was formed during the physical vapor deposition process [63-65]. Second, the insertion of He atoms in the grains but outside of the He bubbles can make a lattice expansion, whose rate would depend upon the solutes. RY Zheng et al. [66] pointed out that most of the implanted He atoms in W do not form He bubbles but may form very small He-vacancy complexes. When He trapping sites are fully occupied, additional He atoms can also form self-clusters [67-69]. In addition, formation of self-interstitial W combined with interstitial He can occur after irradiation [70, 71]. All these structural changes may attribute the lattice expansion. As a simplified system to investigate the effects of solutes on the lattice expansion, we consider W, $W_{89}Ta_{11}$, $W_{89}Re_{11}$ supercells with different concentrations (1.8 to 6.9 %) of He interstitials at the tetrahedral sites for DFT (density functional theory) simulations (*Supporting Information section 2*). We find that the $W_{89}Ta_{11}$ system experiences the smallest lattice expansion after He insertion, followed by the W and $W_{89}Re_{11}$ (Fig. S10(b)). This trend is consistent with the combinatorial experimental results in Fig. 3(b).

The periodicity of the atomic arrangement of the combinatorial specimens has been characterized by determining the FWHM (full width at half maximum) of the (110) peaks of the XRD patterns. Before He-ion irradiation, the W-Re and W-Ta systems have FWHM ranges of $0.30 \sim 0.32^\circ$ and $0.36 \sim 0.47^\circ$, respectively, while the value for the W film is 0.21° (Fig. 3(c)). Therefore, the alloy systems show larger FWHM than pure W, indicating that the insertion of Ta and Re solutes resulted in the reduction of the lattice periodicity (lattice distortion) [72]. Because Ta solute has a larger atomic radius than W (4.26 %), a larger degree of lattice distortion has occurred in the W-Ta system [73]. On the other hand, alloying of W with Re resulted in less change in lattice periodicity since Re atom is smaller than W, and there exists a smaller difference in the atomic radii (2.13 %) between the W and Re atoms. This trend can also be confirmed in FWHM distribution in the un-irradiated W-Re-Ta system (Fig. 3(c)): FWHM is strongly correlated with Ta concentration but not with Re.

After irradiation, the FWHM in all systems increases probably due to the formation of some defects such as vacancy, self-interstitial atoms (SIAs), and He-clusters (Fig. S5(b)). The changes in the FWHM (Fig. 3(d)) of the binary and ternary alloys (4.3 ~ 62.5 %) are smaller than in pure W (93.1 %), suggesting that both the Ta and Re substitutional atoms are helpful for suppressing changes in the periodicity of atomic arrangements. He irradiation on the W-Ta system

involves much smaller changes in FWHM (4.3 ~ 20 %) as compared to other systems. Also, as Ta concentration in the W-Ta-Re alloys increases, the change in the FWHM reduces. The experimental results on the structural periodicity can be compared with the DFT simulation results shown in Fig. S10(c) and (d). That is, after the He insertion to the interstitial sites, FWHM increases for all the supercells of W, W-Ta, and W-Re. Also, the smallest change in FWHM by He is found in the W-Ta system as in the experiment. Meanwhile, from the results of the combinatorial experiment, the composition ranges with small irradiation damages in the FWHM are readily identified in Fig. 3(d): changes in the FWHM of $W_{88-91}Re_{9-12}$, $W_{88-93}Ta_{6-12}$ and $W_{77-82}Re_{9-12}Ta_{9-11}$ are less than half of the pure W case. The intersection composition ranges of low irradiation damages in the lattice parameter and the FWHM can be identified as $W_{89-92}Ta_{8-12}$ and $W_{77-82}Re_{9-12}Ta_{9-11}$.

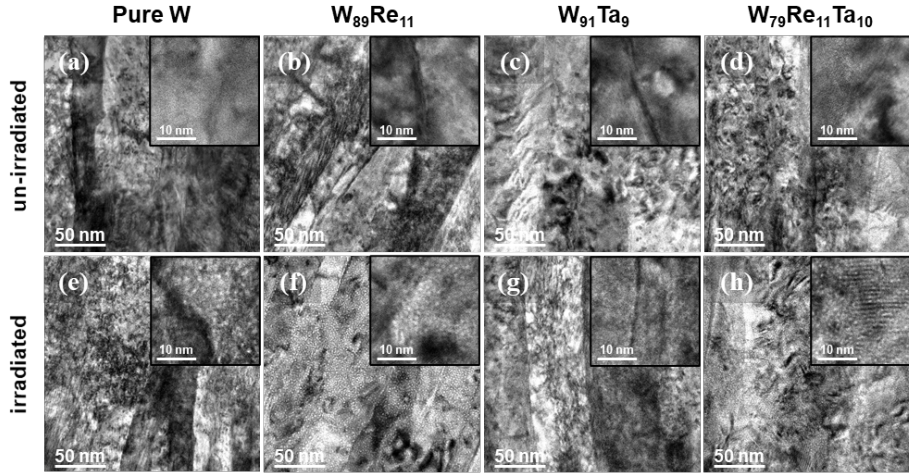


Fig. 4. Cross-sectional bright-field TEM micrographs of (a, e) Pure W, (b, f) $W_{89}Re_{11}$, (c, g) $W_{91}Ta_9$ and (d, h) $W_{79}Re_{11}Ta_{10}$ thin film alloys in (a-d) un-irradiated and (e-h) He-ion irradiated states. Insets show corresponding images with a higher magnification.

Detailed microstructural features of the un-irradiated and irradiated films of W, $W_{89}Re_{11}$, $W_{91}Ta_9$, and $W_{79}Re_{11}Ta_{10}$ have been investigated, as shown in Fig. 4 and Fig. S6-7. The cross-sectional TEM images in Fig. 4 were obtained at a depth of ~ 380 nm of the specimens, where the dpa and He concentrations are expected to be their maxima (Fig. 1(d)). For all the specimens, dense nanocolumnar structures were formed (Fig. S6). The in-plane grain sizes of the specimens determined for un-irradiated W, $W_{89}Re_{11}$, $W_{91}Ta_9$, and $W_{79}Re_{11}Ta_{10}$ films are 53 ± 25 nm, 55 ± 30 nm, 89 ± 35 nm, 57 ± 25 nm, respectively. The largest grain size is found in $W_{91}Ta_9$, which has the largest FWHM of the XRD peak (Fig. 3(c)). Therefore, the large FWHM value in the un-irradiated W-Ta system is not due to a small grain size but lattice distortion as discussed earlier. Formation of large grains in the W-Ta systems can be attributed to the misfit

strain caused by the difference in atomic radii of Ta and W, which leads to an enhanced grain growth rate during the physical vapor deposition process [74].

Fig. 4(e)-(h) displays the TEM micrographs of the He irradiated specimens. The in-plane grain sizes of these specimens were determined for pure W ($55 \pm 27 \text{ nm}$), W-Re ($58 \pm 31 \text{ nm}$), W-Ta ($92 \pm 42 \text{ nm}$) and W-Re-Ta ($63 \pm 27 \text{ nm}$). The changes in the grain sizes after irradiation are negligible. Therefore, the increase in the FWHM after irradiation (Fig. 3(d)) is mainly due to the change in the periodicity of the lattice, caused by the irradiation induced defects. He bubbles are observed in the TEM images of the Pure W, $\text{W}_{89}\text{Re}_{11}$, and $\text{W}_{79}\text{Re}_{11}\text{Ta}_{10}$ films. Many of large He bubbles are found in $\text{W}_{89}\text{Re}_{11}$, while He bubbles might not reach an observable size ($\sim 0.3 \text{ nm}$ [75]) by TEM in W_{91}Ta_9 .

4. Discussion

The irradiation damage maps shown in Fig. 2(b), (d) and in Fig. 3(b), (d) indicate that the addition of Ta in nanostructured W reduces irradiation damages in microstructures and suppresses degradation in the thermal and mechanical properties. The addition of Re also retards the changes in electronic thermal conductivity and in the periodicity of the atomic arrangement after He irradiation, but irradiated W-Re films resulted in rather high irradiation hardening and lattice expansion rates. Here, the effects of Ta and Re solutes in the nanostructured W on the distributions of implanted He, and their roles in the change in the physical properties are discussed.

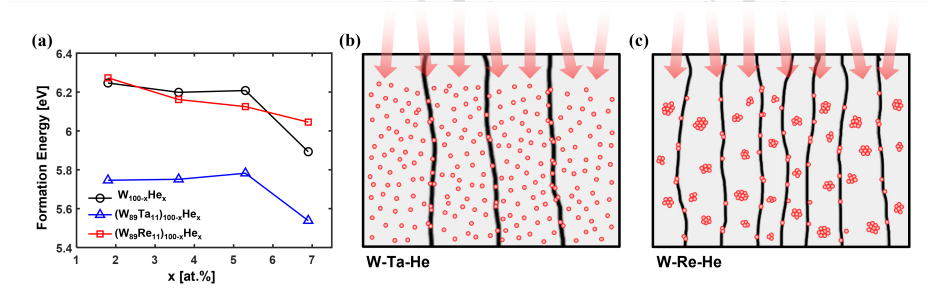


Fig. 5. (a) Formation energies of the interstitial He atoms at the tetrahedral sites in W, $\text{W}_{89}\text{Ta}_{11}$, and $\text{W}_{89}\text{Re}_{11}$ supercells, calculated by DFT simulations. Schematic diagrams representing helium bubble formation in the (b) W-Ta and (c) W-Re microstructures.

To investigate the effect of the solutes on the stability of implanted He, we calculated the formation energies of interstitial He atoms at random tetrahedral sites in pure W and $\text{W}_{89}\text{Ta}_{11}$, $\text{W}_{89}\text{Re}_{11}$ solid-solution supercells by using the DFT simulations (*Supporting Information section 2*). As shown in Fig. 5(a), the interstitial He atoms have the lowest formation energy and are thus most stable in the interstitial sites in the W-Ta system. Also, it has been reported that the activation energy of He diffusion is higher in W-Ta solid-solutions than in W or W-Re systems [76, 77]. Based on these results, it is reasonable to conclude that

implanted He atoms are rather uniformly distributed with smaller cluster sizes in the W-Ta system (Fig. 5(b)), while migration of He atoms and the formation of larger clusters of them is expected for the W-Re system (Fig. 5(c)). In this sense, larger He bubbles are expected to form in the W-Re system, as can be seen from the TEM results (Fig. 4). Besides the effects of the stability and diffusivity of He interstitials, there are other effects to be considered to explain a preferred He bubble formation in the alloys containing Re. Recent studies have shown that the irradiated particles in W-Re alloys enhance the diffusivity of Re atoms, leading to the formation of Re-clusters [78-80]. The Re clusters have high binding energy with He, which enhances the nucleation and growth of He bubbles [76]. Besides, Ta solutes in W-Re-Ta alloys can suppress the formation of the Re-clusters [81, 82]. TEM micrographs of $W_{79}Re_{11}Ta_{10}$ in Fig. 4(h) show that the addition of Ta in W-Re can reduce the He bubble formation significantly.

Different sizes and distributions of He clusters or bubbles due to the Re and Ta solutes lead to different degrees of degradation of the mechanical property. Large He-bubbles in W-Re results in severe irradiation hardening, because the defects interfere dislocation slips effectively [83]. Lower hardening rate, or even softening occurs for the alloys containing Ta, where a much smaller number of He bubbles were formed. For these systems, both hardening and softening mechanisms are expected to be activated: the smaller size and more uniform distribution of He bubbles in W-Ta can suppress dislocation motion and can be dislocation nucleation sources at the same time [84]. The electronic thermal conductivity is also affected by the cluster sizes and the distributions of implanted He in the alloys. Electron scattering occurs more effectively in the specimens with uniformly distributed and high-density small He bubbles (W-Ta, W-Re-Ta), as compared to the samples with larger and lower density He bubbles (W-Re). This argument can be supported by the molecular dynamics (MD) work on Si by T Wang et al. which reported a more significant reduction in the thermal conductivity by uniformly distributed vacancies than by the vacancies clustering [85].

5. Conclusion

In this study, combinatorial experiments for discovering He-irradiation damage tolerant PFMs have been carried out. Combinations of the combinatorial synthesis, a simultaneous He-ion irradiation experiment, and the high-throughput characterizations were used to systematically characterize the irradiation damages of a broad composition range of nanostructured W-Ta-Re alloys. This set of techniques allows a facile identification of the composition ranges with excellent damage tolerance in mechanical ($W_{91}Ta_9$ and $W_{76-83}Re_{10-13}Ta_{7-11}$) and thermal ($W_{89-93}Ta_{7-11}$ and $W_{87-90}Re_{10-13}$) properties, as well as in microstructure ($W_{89-92}Ta_{8-12}$ and $W_{77-82}Re_{9-12}Ta_{9-11}$). It has been revealed that the solutes of Re and Ta in nanostructured W significantly affect the formation and distribution of He-bubbles, which are closely related to the damage behaviors in microstructural and physical properties. We believe that the suggested method can be used to investigate a broader range of damage tolerant nanostructured

alloys with various irradiation conditions, facilitating the discovery of advanced PFMs. Development of the bulk processing would be necessary for the practical application of the nanostructured W-alloys as PFMs.

Acknowledgements

This research was supported by Basic Science Research Program through the National Research Foundation of Korea (NRF) funded by the Ministry of Science, ICT and Future Planning (NRF-2017R1E1A1A01078324, NRF-2020M3D1A1016092).

Data availability

The raw and processed data required to reproduce these findings are available from the corresponding author upon reasonable request.

6. References

- [1] J. Knaster, A. Moeslang, T. Muroga, Materials research for fusion, *Nature Physics* 12(5) (2016) 424-434.
- [2] JW Davis, VR Barabash, A Makhankov, L. Ploch, Assessment of tungsten for use in the ITER plasma facing components, *Journal of Nuclear Materials* 258-263 (1998) 308-312.
- [3] J.N. Brooks, L. El-Guebaly, A. Hassanein, T. Sizyuk, Plasma-facing material alternatives to tungsten, *Nuclear Fusion* 55(4) (2015).
- [4] R. Causey, K. Wilson, T. Venhaus, W.R. Wampler, Tritium retention in tungsten exposed to intense fluxes of 100 eV tritons, *Journal of Nuclear Materials* 266-269 (1999) 467-471.
- [5] Z. Zhou, J. Linke, G. Pintsuk, J. Du, S. Song, C. Ge, High heat load properties of ultra fine grained tungsten, *Journal of Nuclear Materials* 386-388 (2009) 733-735.
- [6] G.-M. Song, Y.-J. Wang, Y. Zhou, The mechanical and thermophysical properties of ZrC/W composites at elevated temperature, *Materials Science and Engineering: A* 334(1-2) (2002) 223-232.
- [7] X. Hu, T. Koyanagi, M. Fukuda, N.A.P.K. Kumar, L.L. Snead, B.D. Wirth, Y. Katoh, Irradiation hardening of pure tungsten exposed to neutron irradiation, *Journal of Nuclear Materials* 480 (2016) 235-243.
- [8] A. Hasegawa, M. Fukuda, K. Yabuuchi, S. Nogami, Neutron irradiation effects on the microstructural development of tungsten and tungsten alloys, *Journal of Nuclear Materials* 471 (2016) 175-183.
- [9] Y. Ueda, J. Coenen, G. De Temmerman, R. Doerner, J. Linke, V. Philipps, E. Tsiganeas, Research status and issues of tungsten plasma facing materials for ITER and beyond, *Fusion Engineering and Design* 89(7-8) (2014) 901-906.

- [10] N. Yoshida, H. Iwakiri, K. Tokunaga, T. Baba, Impact of low energy helium irradiation on plasma facing metals, *Journal of Nuclear Materials* 337-339 (2005) 946-950.
- [11] J. Yu, W. Han, Z. Chen, K. Zhu, Blistering of tungsten films deposited by magnetron sputtering after helium irradiation, *Fusion Engineering and Design* 129 (2018) 230-235.
- [12] A. Al-Ajlony, J.K. Tripathi, A. Hassanein, Low energy helium ion irradiation induced nanostructure formation on tungsten surface, *Journal of Nuclear Materials* 488 (2017) 1-8.
- [13] Y. Nobuta, Y. Hatano, M. Matsuyama, S. Abe, Y. Yamauchi, T. Hino, Helium irradiation effects on tritium retention and long-term tritium release properties in polycrystalline tungsten, *Journal of Nuclear Materials* 463 (2015) 993-996.
- [14] B.D. Wirth, K.D. Hammond, S.I. Krasheninnikov, D. Maroudas, Challenges and opportunities of modeling plasma-surface interactions in tungsten using high-performance computing, *Journal of Nuclear Materials* 463 (2015) 30-38.
- [15] M. Wirtz, J. Linke, G. Pintsuk, L. Singheiser, I. Uytendhouwen, Comparison of the thermal shock performance of different tungsten grades and the influence of microstructure on the damage behaviour, *Physica Scripta* T145 (2011).
- [16] I. Ipatova, G. Greaves, S. Pacheco-Gutiérrez, S.C. Middleburgh, M.J.D. Rushton, E. Jimenez-Melero, In-situ TEM investigation of nano-scale helium bubble evolution in tantalum-doped tungsten at 800°C, *Journal of Nuclear Materials* 550 (2021).
- [17] S. Gonderman, J.K. Tripathi, T.J. Novakowski, T. Sizyuk, A. Hassanein, The effect of low energy helium ion irradiation on tungsten-tantalum (W-Ta) alloys under fusion relevant conditions, *Journal of Nuclear Materials* 491 (2017) 199-205.
- [18] Y. MUTOH., K. ICHIKAWA, K. NAGATA, M. TAKEUCHI, Effect of rhenium addition on fracture toughness of tungsten at elevated temperatures, *Journal of Materials Science* 30 (1995) 770-775.
- [19] M. Fukuda, T. Tanno, S. Nogami, A. Hasegawa, Effects of Re Content and Fabrication Process on Microstructural Changes and Hardening in Neutron Irradiated Tungsten, *Materials Transactions* 53(12) (2012) 2145-2150.
- [20] Z. Chen, L.-L. Niu, Z. Wang, L. Tian, L. Kecskes, K. Zhu, Q. Wei, A comparative study on the in situ helium irradiation behavior of tungsten: Coarse grain vs. nanocrystalline grain, *Acta Materialia* 147 (2018) 100-112.
- [21] T. Lifeng, L. Pei, L. Xuanze, M. Yutian, M. Xiangmin, Cracks and blisters formed in nanocrystalline tungsten films by helium implantation, *Fusion Engineering and Design* 172 (2021).

- [22] I. Oh, D. Park, E. Cheong, H. Jo, S. Park, D. You, T. Kim, Y. Park, K. Kim, G.-D. Sim, C. Shin, D. Lee, Anisotropic He-ion irradiation damages in nanocolumnar W thin films, *Extreme Mechanics Letters* 41 (2020).
- [23] W. Qin, F. Ren, R.P. Doerner, G. Wei, Y. Lv, S. Chang, M. Tang, H. Deng, C. Jiang, Y. Wang, Nanochannel structures in W enhance radiation tolerance, *Acta Materialia* 153 (2018) 147-155.
- [24] W. Qin, Y. Wang, M. Tang, F. Ren, Q. Fu, G. Cai, L. Dong, L. Hu, G. Wei, C. Jiang, Microstructure and hardness evolution of nanochannel W films irradiated by helium at high temperature, *Journal of Nuclear Materials* 502 (2018) 132-140.
- [25] W. Qin, S. Jin, X. Cao, Y. Wang, P. Peres, S.-Y. Choi, C. Jiang, F. Ren, Influence of nanochannel structure on helium-vacancy cluster evolution and helium retention, *Journal of Nuclear Materials* 527 (2019).
- [26] S. Si, W. Li, X. Zhao, M. Han, Y. Yue, W. Wu, S. Guo, X. Zhang, Z. Dai, X. Wang, X. Xiao, C. Jiang, Significant Radiation Tolerance and Moderate Reduction in Thermal Transport of a Tungsten Nanofilm by Inserting Monolayer Graphene, *Adv Mater* 29(3) (2017).
- [27] O. El-Atwani, N. Li, M. Li, A. Devaraj, J.K.S. Baldwin, M.M. Schneider, D. Sobieraj, J.S. Wróbel, D. Nguyen-Manh, S.A. Maloy, E. Martinez, Outstanding radiation resistance of tungsten-based high-entropy alloys, *Science Advances* 5(3) (2019) eaav2002.
- [28] Y.C. Wu, Q.Q. Hou, L.M. Luo, X. Zan, X.Y. Zhu, P. Li, Q. Xu, J.G. Cheng, G.N. Luo, J.L. Chen, Preparation of ultrafine-grained/nanostructured tungsten materials: An overview, *Journal of Alloys and Compounds* 779 (2019) 926-941.
- [29] Y. Xu, C. Xie, S. Qin, J. Song, Q. Li, S. Zhao, G. Liu, T. Wang, Y. Yu, G. Luo, Preliminary R&D on flat-type W/Cu plasma-facing materials and components for Experimental Advanced Superconducting Tokamak, *Physica Scripta* 2014(T159) (2014) 014008.
- [30] N. Sun, S. Lang, Y. Zhang, Y. Xu, H. Liu, G. Li, Properties of electrodeposited tungsten coatings on graphite substrates for plasma facing components, *Journal of Fusion Energy* 35(4) (2016) 660-665.
- [31] R. Potyrailo, K. Rajan, K. Stoewe, I. Takeuchi, B. Chisholm, H. Lam, Combinatorial and high-throughput screening of materials libraries: review of state of the art, *ACS Comb Sci* 13(6) (2011) 579-633.
- [32] A. Ludwig, Discovery of new materials using combinatorial synthesis and high-throughput characterization of thin-film materials libraries combined with computational methods, *npj Computational Materials* 5(1) (2019).
- [33] D. You, H. Zhang, S. Ganorkar, T. Kim, J. Schroers, J.J. Vlassak, D. Lee, Electrical resistivity as a descriptor for classification of amorphous versus crystalline phases of alloys, *Acta Materialia* 231 (2022) 117861.

- [34] K. Kim, S. Park, T. Kim, Y. Park, G.-D. Sim, D. Lee, Mechanical, Electrical Properties and Microstructures of Combinatorial Ni-Mo-W alloy films, *Journal of Alloys and Compounds* (2022) 165808.
- [35] W. Jiang, Y. Zhu, L. Zhang, D.J. Edwards, N.R. Overman, G. Nandipati, W. Setyawan, C.H. Henager Jr, R.J. Kurtz, Dose rate effects on damage accumulation and void growth in self-ion irradiated tungsten, *Journal of Nuclear Materials* 550 (2021) 152905.
- [36] M. Seo, K. Wang, J.R. Echols, A.L. Winfrey, Microstructure deformation and near-pore environment of resolidified tungsten in high heat flux conditions, *Journal of Nuclear Materials* 565 (2022) 153725.
- [37] S. Wang, W. Guo, Y. Yuan, N. Gao, X. Zhu, L. Cheng, X. Cao, E. Fu, L. Shi, F. Gao, Evolution of vacancy defects in heavy ion irradiated tungsten exposed to helium plasma, *Journal of Nuclear Materials* 532 (2020) 152051.
- [38] D.S. Perloff, Four-point sheet resistance correction factors for thin rectangular samples, *Solid-State Electronics* 20(8) (1977) 681-687.
- [39] I. Miccoli, F. Edler, H. Pfnur, C. Tegenkamp, The 100th anniversary of the four-point probe technique: the role of probe geometries in isotropic and anisotropic systems, *J Phys Condens Matter* 27(22) (2015) 223201.
- [40] R. Franz, G. Wiedemann, Ueber die Wärme-Leitungsfähigkeit der Metalle, *Annalen der Physik* 165(8) (1853) 497-531.
- [41] B. Fu, W. Lai, Y. Yuan, H. Xu, W. Liu, Calculation and analysis of lattice thermal conductivity in tungsten by molecular dynamics, *Journal of Nuclear Materials* 427(1-3) (2012) 268-273.
- [42] S. Cui, M. Simmonds, W. Qin, F. Ren, G.R. Tynan, R.P. Doerner, R. Chen, Thermal conductivity reduction of tungsten plasma facing material due to helium plasma irradiation in PISCES using the improved 3-omega method, *Journal of Nuclear Materials* 486 (2017) 267-273.
- [43] W.C. Oliver, G.M. Pharr, An improved technique for determining hardness and elastic modulus using load and displacement sensing indentation experiments, *Journal of Materials Research* 7(6) (1992) 1564-1583.
- [44] A. Fischer-Cripps, A review of analysis methods for sub-micron indentation testing, *Vacuum* 58(4) (2000) 569-585.
- [45] X. Cai, H. Bangert, Hardness measurements of thin films-determining the critical ratio of depth to thickness using FEM, *Thin Solid Films* 264(1) (1995) 59-71.
- [46] N. Astm, Standard practice for neutron radiation damage simulation by charged-particle irradiation, *Annu. B. ASTM Stand.* 12 (1996) E521.
- [47] M.J. Banisalman, S. Park, T. Oda, Evaluation of the threshold displacement energy in tungsten by molecular dynamics calculations, *Journal of Nuclear*

Materials 495 (2017) 277-284.

- [48] J.A. Thornton, High rate thick film growth, *Annual review of materials science* 7(1) (1977) 239-260.
- [49] O. El-Atwani, K. Hattar, J.A. Hinks, G. Greaves, S.S. Harilal, A. Hassanein, Helium bubble formation in ultrafine and nanocrystalline tungsten under different extreme conditions, *Journal of Nuclear Materials* 458 (2015) 216-223.
- [50] G. Wei, J. Li, Y. Li, H. Deng, C. Jiang, F. Ren, A better nanochannel tungsten film in releasing helium atoms, *Journal of Nuclear Materials* 532 (2020).
- [51] F. Zhu, D. Wang, N. Gao, H. Peng, Z. Xie, Z. Zhang, Microstructure evolution and Young's modulus of He-implanted nanocrystalline tungsten film, *Journal of Nuclear Materials* 518 (2019) 226-233.
- [52] Z. Shang, J. Ding, C. Fan, D. Chen, J. Li, Y. Zhang, Y. Wang, H. Wang, X. Zhang, He ion irradiation response of a gradient T91 steel, *Acta Materialia* 196 (2020) 175-190.
- [53] A. Luo, D.L. Jacobson, K.S. Shin, Solution softening mechanism of iridium and rhenium in tungsten at room temperature, *International Journal of Refractory Metals and Hard Materials* 10(2) (1991) 107-114.
- [54] J.R. Stephens, W.R. Witzke, Alloy softening in group via metals alloyed with rhenium, *Journal of the Less Common Metals* 23(4) (1971) 325-342.
- [55] J. Stephens, Dislocation structure in single-crystal tungsten and tungsten alloys, *Metallurgical and Materials Transactions B* 10(1) (1970) 1293.
- [56] E. Tejado, P.A. Carvalho, A. Munoz, M. Dias, J.B. Correia, U.V. Mardolcar, J.Y. Pastor, The effects of tantalum addition on the microtexture and mechanical behaviour of tungsten for ITER applications, *Journal of Nuclear Materials* 467 (2015) 949-955.
- [57] Z. Wang, Y. Yuan, K. Arshad, J. Wang, Z. Zhou, J. Tang, G.-H. Lu, Effects of tantalum concentration on the microstructures and mechanical properties of tungsten-tantalum alloys, *Fusion Engineering and Design* 125 (2017) 496-502.
- [58] J. Li, B. Lu, Y. Zhang, H. Zhou, G. Hu, R. Xia, Nanoindentation response of nanocrystalline copper via molecular dynamics: Grain-size effect, *Materials Chemistry and Physics* 241 (2020).
- [59] F. Hofmann, D.R. Mason, J.K. Eliason, A.A. Maznev, K.A. Nelson, S.L. Dudarev, Non-Contact Measurement of Thermal Diffusivity in Ion-Implanted Nuclear Materials, *Sci Rep* 5 (2015) 16042.
- [60] R. Taylor, R. Finch, The specific heats and resistivities of molybdenum, tantalum, and rhenium, *Journal of the Less Common Metals* 6(4) (1964) 283-294.
- [61] M. Zhao, W. Pan, C. Wan, Z. Qu, Z. Li, J. Yang, Defect engineering in development of low thermal conductivity materials: A review, *Journal of the European Ceramic Society* 37(1) (2017) 1-13.

- [62] C. Kittel, Introduction to Solid State Physics, 6th edition, Wiley, New York 1986.
- [63] A. Debelle, A. Michel, G. Abadias, C. Jaouen, Ion-irradiation induced stress relaxation in metallic thin films and multilayers grown by ion beam sputtering, Nuclear Instruments and Methods in Physics Research Section B: Beam Interactions with Materials and Atoms 242(1-2) (2006) 461-465.
- [64] A. Debelle, G. Abadias, A. Michel, C. Jaouen, V. Pelosin, Growth stress buildup in ion beam sputtered Mo thin films and comparative study of stress relaxation upon thermal annealing or ion irradiation, Journal of Vacuum Science & Technology A: Vacuum, Surfaces, and Films 25(5) (2007).
- [65] K. Hlushko, A. Mackova, J. Zalesak, M. Burghammer, A. Davydok, C. Krywka, R. Daniel, J. Keckes, J. Todt, Ion irradiation-induced localized stress relaxation in W thin film revealed by cross-sectional X-ray nanodiffraction, Thin Solid Films 722 (2021).
- [66] R.-Y. Zheng, W.-R. Jian, I.J. Beyerlein, W.-Z. Han, Atomic-scale hidden point-defect complexes induce ultrahigh-irradiation hardening in tungsten, Nano Letters 21(13) (2021) 5798-5804.
- [67] C.S. Becquart, C. Domain, Migration energy of He in W revisited by ab initio calculations, Phys Rev Lett 97(19) (2006) 196402.
- [68] W. Wilson, Theory of small clusters of helium in metals, Radiation Effects 78(1-4) (1983) 11-24.
- [69] Y.-W. You, D. Li, X.-S. Kong, X. Wu, C. Liu, Q. Fang, B. Pan, J. Chen, G.-N. Luo, Clustering of H and He, and their effects on vacancy evolution in tungsten in a fusion environment, Nuclear Fusion 54(10) (2014) 103007.
- [70] Y.-W. You, J. Sun, X.-S. Kong, X. Wu, Y. Xu, X. Wang, Q. Fang, C. Liu, Effects of self-interstitial atom on behaviors of hydrogen and helium in tungsten, Physica Scripta 95(7) (2020) 075708.
- [71] Y.-W. You, J. Sun, X.-S. Kong, X. Wu, Y. Xu, X.P. Wang, Q.F. Fang, C.S. Liu, Effects of self-interstitial atom on behaviors of hydrogen and helium in tungsten, Physica Scripta 95(7) (2020).
- [72] T. Ungár, Microstructural parameters from X-ray diffraction peak broadening, Scripta Materialia 51(8) (2004) 777-781.
- [73] Z. Guo, L. Wang, X.-Z. Wang, Additive manufacturing of W-12Ta(wt%) alloy: Processing and resulting mechanical properties, Journal of Alloys and Compounds 868 (2021) 159193.
- [74] G. Kim, X. Chai, L. Yu, X. Cheng, D.S. Gianola, Interplay between grain boundary segregation and electrical resistivity in dilute nanocrystalline Cu alloys, Scripta Materialia 123 (2016) 113-117.

- [75] D. Chen, Y. Tong, H. Li, J. Wang, Y.L. Zhao, A. Hu, J.J. Kai, Helium accumulation and bubble formation in FeCoNiCr alloy under high fluence He+ implantation, *Journal of Nuclear Materials* 501 (2018) 208-216.
- [76] F.-Y. Yue, Y.-H. Li, Q.-Y. Ren, F.-F. Ma, Z.-Z. Li, H.-B. Zhou, H. Deng, Y. Zhang, G.-H. Lu, Suppressing/enhancing effect of rhenium on helium clusters evolution in tungsten: Dependence on rhenium distribution, *Journal of Nuclear Materials* 543 (2021).
- [77] Y. Chen, J. Fang, X. Liao, N. Gao, W. Hu, H.-B. Zhou, H. Deng, Energetics and diffusional properties of helium in W-Ta systems studied by a new ternary potential, *Journal of Nuclear Materials* 549 (2021).
- [78] T. Hwang, A. Hasegawa, K. Tomura, N. Ebisawa, T. Toyama, Y. Nagai, M. Fukuda, T. Miyazawa, T. Tanaka, S. Nogami, Effect of neutron irradiation on rhenium cluster formation in tungsten and tungsten-rhenium alloys, *Journal of Nuclear Materials* 507 (2018) 78-86.
- [79] J. Fu, Y. Chen, J. Fang, N. Gao, W. Hu, C. Jiang, H.-B. Zhou, G.-H. Lu, F. Gao, H. Deng, Molecular dynamics simulations of high-energy radiation damage in W and W-Re alloys, *Journal of Nuclear Materials* 524 (2019) 9-20.
- [80] C.-H. Huang, L. Gharaee, Y. Zhao, P. Erhart, J. Marian, Mechanism of nucleation and incipient growth of Re clusters in irradiated W-Re alloys from kinetic Monte Carlo simulations, *Physical Review B* 96(9) (2017).
- [81] A. Xu, D.E.J. Armstrong, C. Beck, M.P. Moody, G.D.W. Smith, P.A.J. Bagot, S.G. Roberts, Ion-irradiation induced clustering in W-Re-Ta, W-Re and W-Ta alloys: An atom probe tomography and nanoindentation study, *Acta Materialia* 124 (2017) 71-78.
- [82] Y.-W. You, X.-S. Kong, X. Wu, C.S. Liu, Q.F. Fang, J.L. Chen, G.N. Luo, Clustering of transmutation elements tantalum, rhenium and osmium in tungsten in a fusion environment, *Nuclear Fusion* 57(8) (2017).
- [83] M.H. Cui, Z.G. Wang, L.L. Pang, T.L. Shen, C.F. Yao, B.S. Li, J.Y. Li, X.Z. Cao, P. Zhang, J.R. Sun, Y.B. Zhu, Y.F. Li, Y.B. Sheng, Temperature dependent defects evolution and hardening of tungsten induced by 200keV He-ions, *Nuclear Instruments and Methods in Physics Research Section B: Beam Interactions with Materials and Atoms* 307 (2013) 507-511.
- [84] W.S. Cunningham, J.M. Gentile, O. El-Atwani, C.N. Taylor, M. Efe, S.A. Maloy, J.R. Trelewicz, Softening due to Grain Boundary Cavity Formation and its Competition with Hardening in Helium Implanted Nanocrystalline Tungsten, *Sci Rep* 8(1) (2018) 2897.
- [85] T. Wang, G.K.H. Madsen, A. Hartmaier, Atomistic study of the influence of lattice defects on the thermal conductivity of silicon, *Modelling and Simulation in Materials Science and Engineering* 22(3) (2014).

Combinatorial Discovery of Irradiation Damage Tolerant Nano-structured W-based alloys

Haechan Jo ^a, Sanghun Park ^a, Daegun You ^a, Sooran Kim ^b, Dongwoo Lee ^{a, *}

^a School of Mechanical Engineering, Sungkyunkwan University (SKKU), Suwon 16419, Republic of Korea

^b Department of Physics Education, Kyungpook National University (KNU), Daegu 41944, Republic of Korea

*Corresponding Authors Email: dongwoolee@skku.edu

1. Physical properties and microstructures of the combinatorial thin film alloys

The mechanical, electrical, thermal properties, XRD results, TEM micrographs that are not shown in the manuscript are presented in Fig. S1-7.

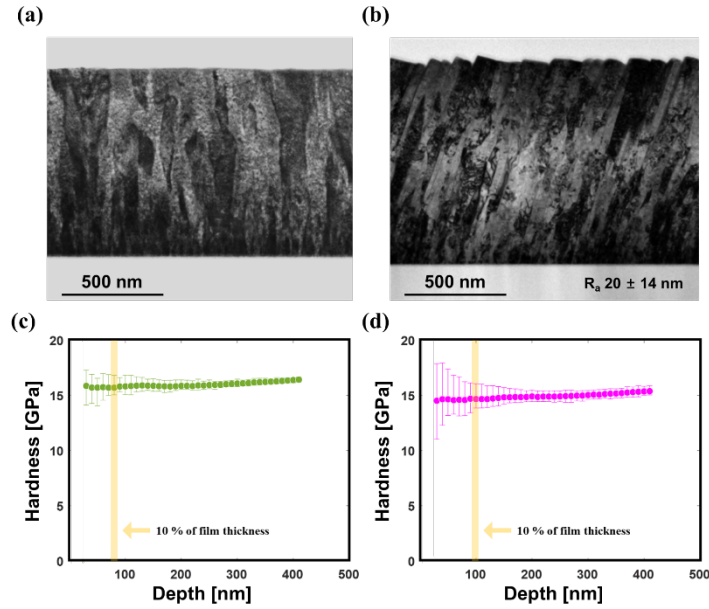


Fig. S1. Cross-sectional TEM micrographs of pure W films (a) with a smooth surface and (b) a rough surface ($R_a = 20 \pm 14$ nm). (c, d) Nano-indentation hardness vs. depth graphs for the samples in (a) and (b), respectively.

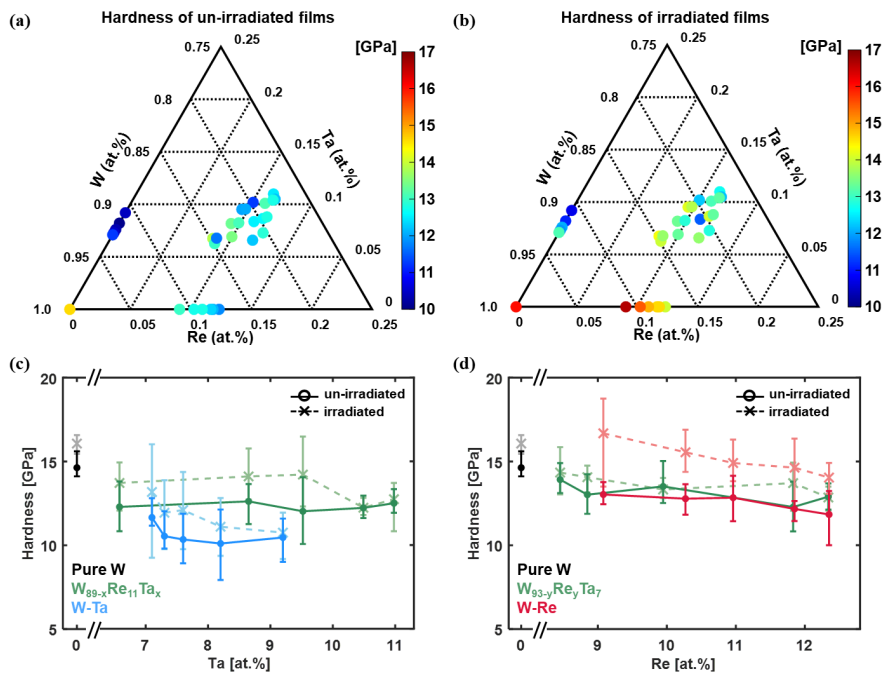


Fig. S2. The nanoindentation hardness maps of the (a) un-irradiated and (b) irradiated combinatorial films. (c, d) Hardness of selected compositions of the W-Ta, W-Re, and W-Re-Ta systems are shown with error bars.

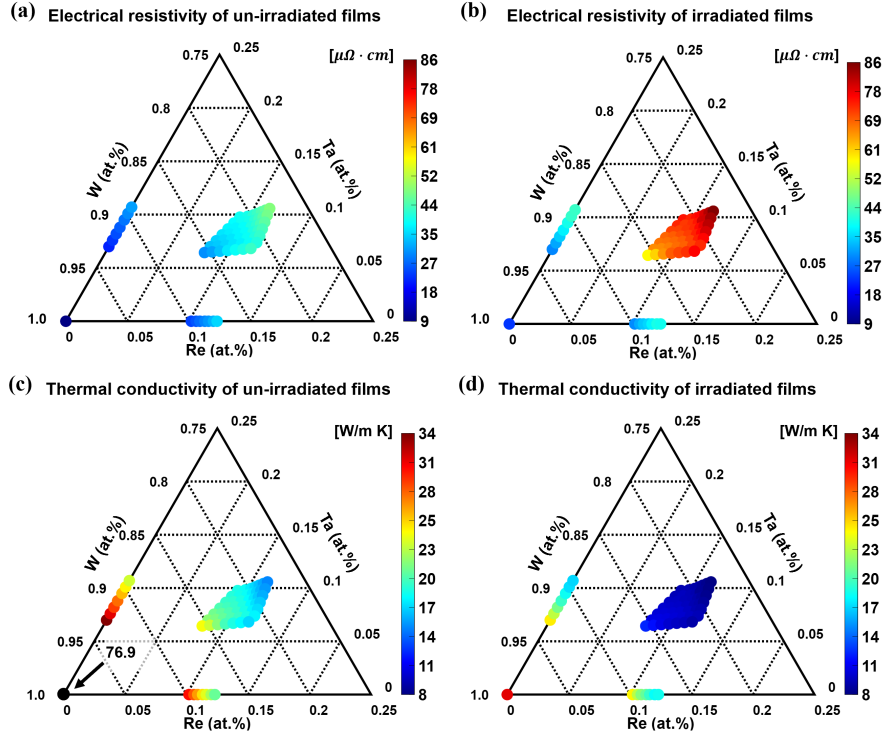


Fig. S3. Electrical resistivity maps of the (a) un-irradiated and (b) irradiated combinatorial films. Electronic thermal conductivity maps of the (c) un-irradiated and (d) irradiated films.

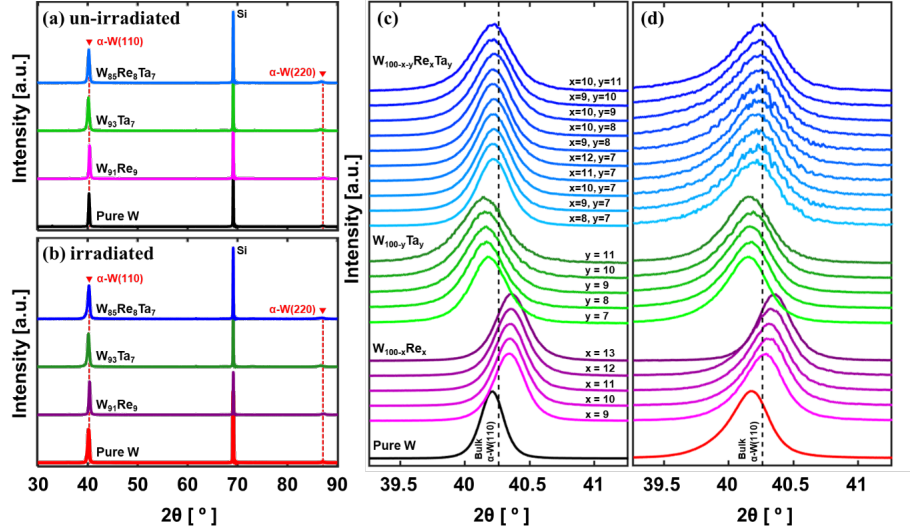


Fig. S4. XRD spectra of some of the (a) un-irradiated and (b) irradiated films. A magnified view of the (110) peaks of the (c) un-irradiated and (d) irradiated films with selected compositions of the W, W-Re, W-Ta, and W-Re-Ta systems. The lattice parameter of un-irradiated pure W film was determined as 3.1678 Å (c), which can be compared with the bulk value of 3.1648 Å. This difference gives 0.095% of the out-of-plane residual strain, which corresponds to -0.135 % of in-plane residual strain and -0.60 GPa of in-plane residual stress.

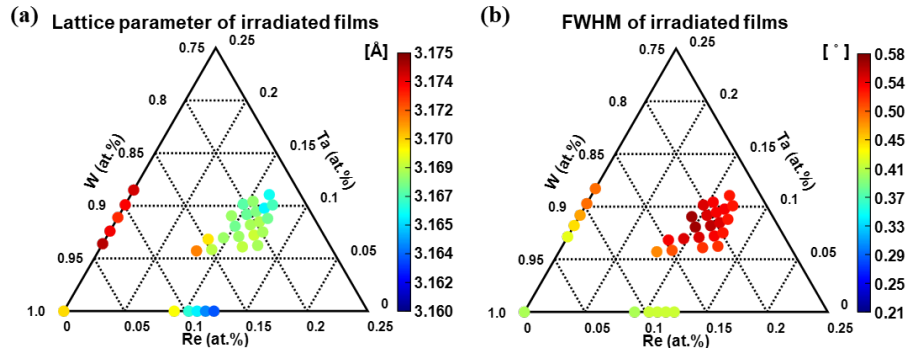


Fig. S5. (a) The lattice parameter map and (b) the FWHM (full width at half maximum) map determined from the (110) XRD peaks of the irradiated films.

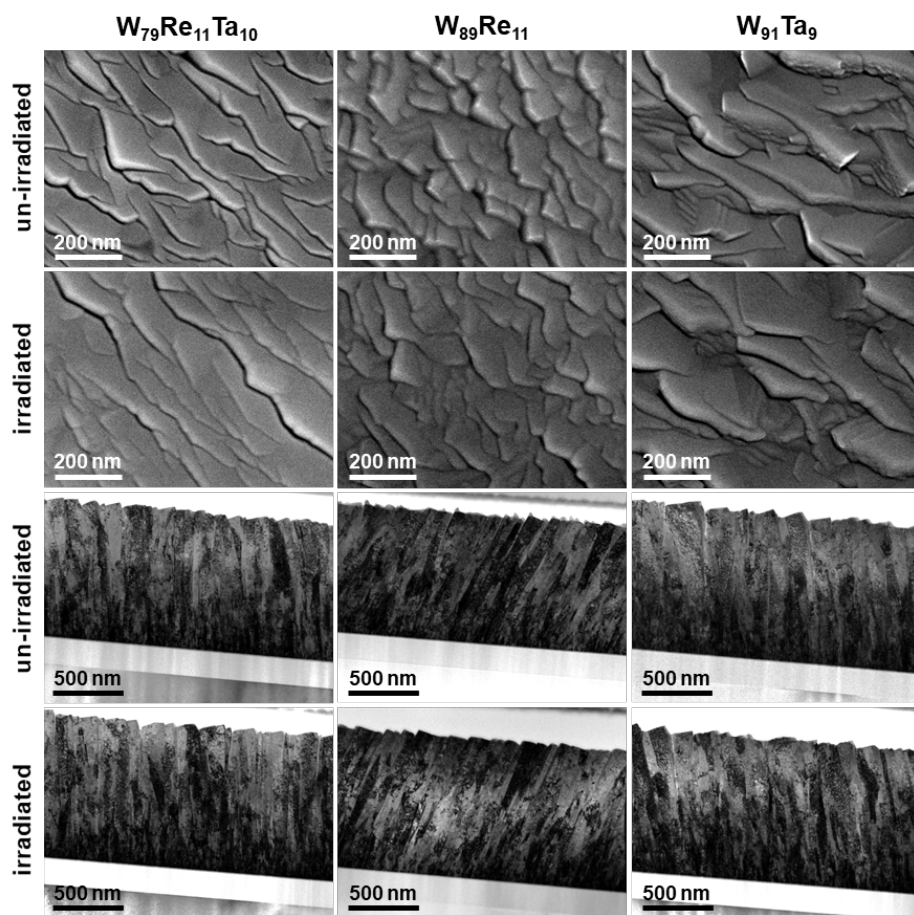


Fig. S6. Surface SEM (top two rows) and bright-field cross-sectional TEM (bottom two rows) images of the Pure W, $W_{89}Re_{11}$, $W_{91}Ta_9$ and $W_{79}Re_{11}Ta_{10}$ specimens.

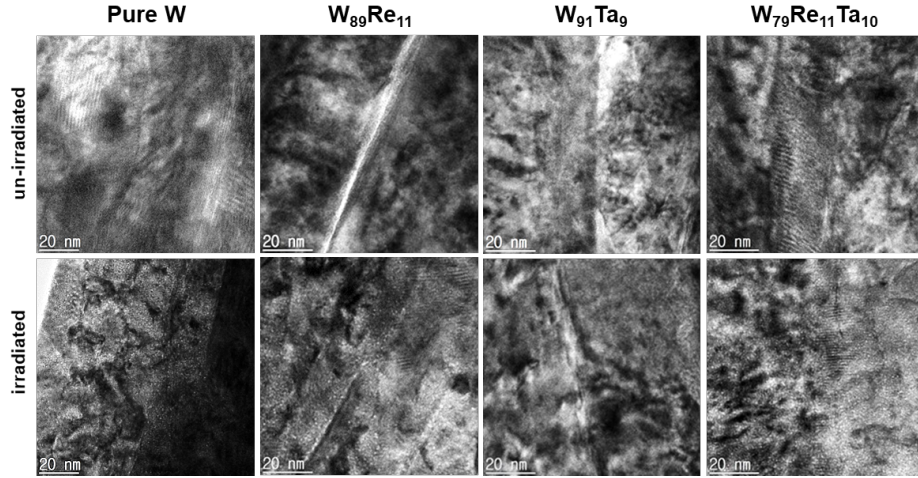


Fig. S7. Cross-sectional TEM micrographs of the Pure W, $W_{89}Re_{11}$, $W_{91}Ta_9$ and $W_{79}Re_{11}Ta_{10}$ films at high magnifications.

2. First-principles calculations

2-1. Stabilities of the Ta and Re solutes, and He interstitials

In this section, we investigate the stabilities of substitutional Ta and Re atoms, as well as the interstitial He atom by calculating formation energies (E_f) of each of the atoms. The W supercell before inserting any point defect is composed of $3 \times 3 \times 3$ BCC unit cells with a lattice constant of 3.185 Å (a total of 54 host atoms). We then inserted the Ta or Re atom to a substitutional position (Fig. S8(a)) and relaxed the structure. Similarly, a He atom was inserted to the tetrahedral interstitial site (TIS) or octahedral interstitial site (OIS) (Fig. S8(b) and (c)). The created structures were relaxed by DFT simulations as described in *Experimental section*.

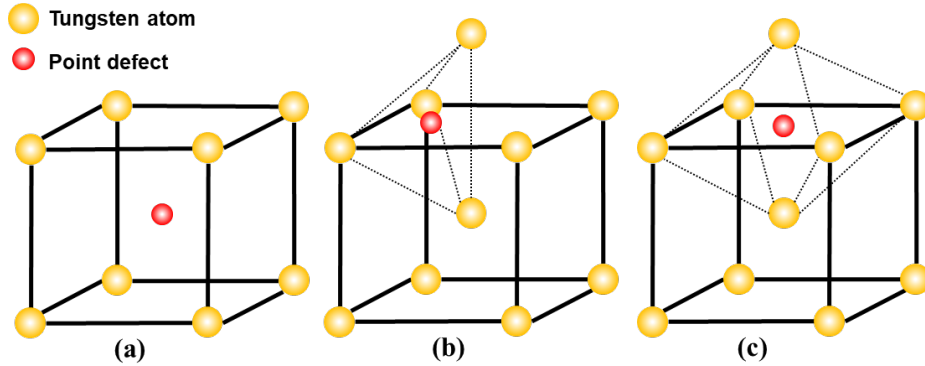


Fig. S8. Schematic illustrates of the atomic positions of (a) the substitutional site and the (b) tetrahedral, (c) octahedral interstitial sites.

The formation energies of each structure were then calculated by using:

$$\underline{E_f = E_{\text{tot}}^X - E_{\text{tot}}^P - \sum_i n_i \mu_i} \quad [2], \quad (\text{Equation S1})$$

where E_{tot}^X is the total energies of the relaxed supercell including the point defect, E_{tot}^P is the total energies of the crystal without any defect (pure W), μ_i is the chemical potential of element species i , and n_i is the number of elements of species i added to ($n_i > 0$) or removed from ($n_i < 0$) the supercell. The adopted chemical potential for W, Ta, Re, and He are -12.96, -11.85, -12.44 eV and -0.0071 eV, respectively [3]. The formation energies of substitutional Ta (Ta_{Sub}) and Re (Re_{Sub}) respectively were calculated as -0.44 and 0.25 eV. The calculated formation energies of the interstitial He at OIS (He_{OIS}) and at TIS (He_{TIS}) are 6.45 and 6.24 eV. These results agree reasonably well with references (Table S1).

Table S1. Formation energies (eV) of the point defects in W.

	Ta_{Sub}	Re_{Sub}	He_{OIS}	He_{TIS}
Present study	- 0.44	0.25	6.45	6.24
Reference [2]	-	-	6.39	6.26
Reference [4]	-0.45	0.18	6.18	-
Reference [5]	-0.47	0.17	-	-
Reference [6]	-	-	6.48	6.23
Reference [7]	-	-	6.42	6.19

Next, structures with higher solute (Ta or Re) concentrations were created by inserting six of solutes at random positions of the W supercell, making the overall solute concentration of 11 %. For the W, $W_{89}Ta_{11}$, and $W_{89}Re_{11}$ supercells, He atoms were inserted to random TIS as it is more stable than OIS (Table S1). The number of He atoms inserted varied from one to four, making the overall He concentration from 1.8 to 6.9 %. The formation energies of the interstitial He in the W, $W_{89}Ta_{11}$, and $W_{89}Re_{11}$ systems can be calculated by:

$$\underline{E_f = (E_{\text{tot}}^{W_{54-m}Sol_m He_n} - E_{\text{tot}}^{W_{54-m}Sol_m} - n_{He} \bullet \mu_{He})/n_{He}} \quad [8], \quad (\text{Equation S2})$$

where $E_{\text{tot}}^{W_{54-m}Sol_m He_n}$ and $E_{\text{tot}}^{W_{54-m}Sol_m}$ are the total energies of the supercells with and without TIS He atoms in the $W_{54-m}Sol_m$ systems and m , n_{He} represent the numbers of the solutes and He atoms ($m = 0$, for the pure W case), respectively. Calculated E_f as a function of He concentration can be seen in manuscript (see Fig. 5(a)).

2-2. Structural analyses

For the relaxed structures of $W_{100-x}He_x$, $(W_{89}Ta_{11})_{100-x}He_x$, $(W_{89}Re_{11})_{100-x}$,

radial distribution functions (RDFs) were determined as shown in Fig. S9. From the second peak of the RDF, the lattice parameter of the bcc structure can be determined (Fig. S9(a)). Also, the periodicity of the lattice can be analyzed by calculating the FWHM (full width at half maximum) of an RDF peak. Considering the second peak for the FWHM calculations, we find that the FWHM increases as the concentration of interstitial He increases (Fig. S9(b) ~ (d)).

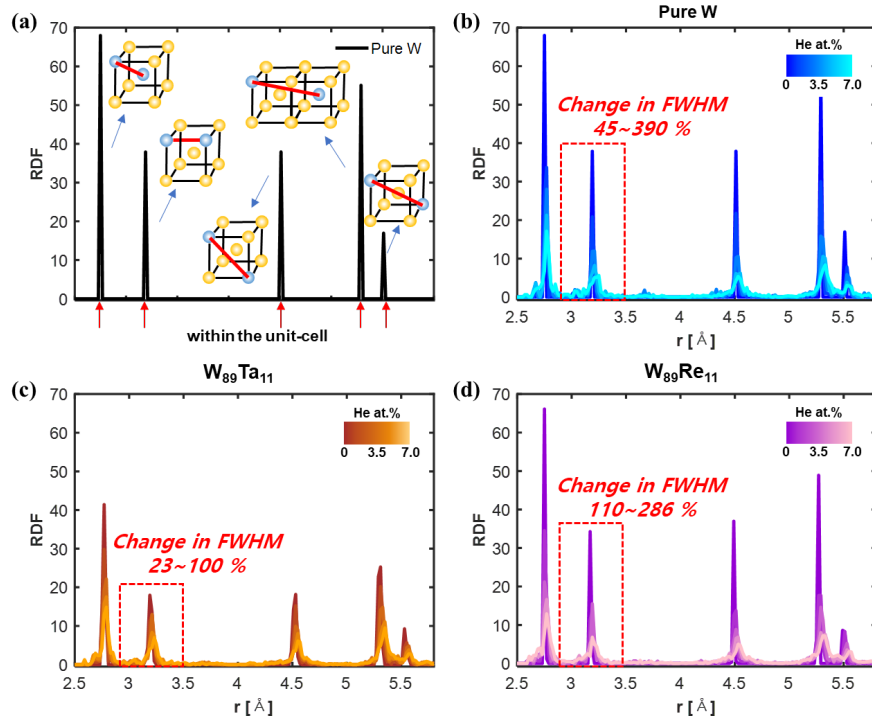


Fig. S9. RDF curves of (a) Pure W, (b) $W_{100-x}He_x$, (c) $(W_{89}Ta_{11})_{100-x}He_x$ and (d) $(W_{89}Re_{11})_{100-x}$.

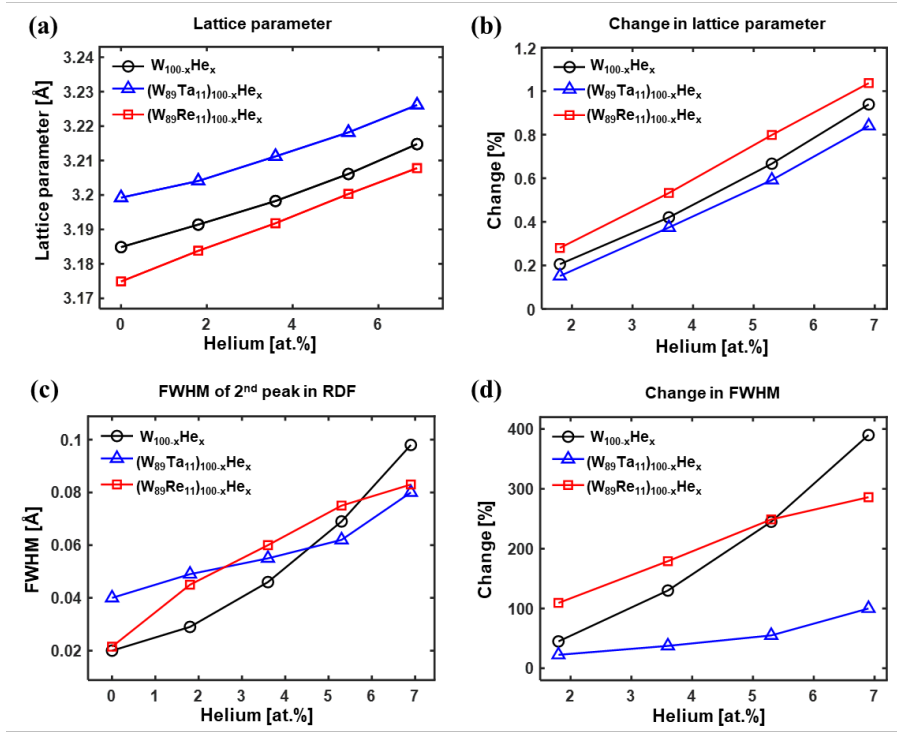


Fig. S10. (a) The lattice parameter, (b) the change in the lattice parameter, (c) the FWHM, and (d) the change in FWHM of $W_{100-x}He_x$, $(W_{89}Ta_{11})_{100-x}He_x$, and $(W_{89}Re_{11})_{100-x}$ supercells.

The calculated lattice parameters and the FWHM from the RDF curves are shown in Fig. S9 and S10. Before insertion of any He atoms, $W_{89}Ta_{11}$ has the largest lattice parameter (3.199 Å), followed by pure W (3.185 Å) and $W_{89}Re_{11}$ (3.175 Å) (Fig. S10(a)). As the interstitial He atoms at TIS are inserted, lattice swelling occurs for all the systems considered (Fig. S10(a)). The change rate in the lattice parameter due to He insertion is found smallest in the $W_{89}Ta_{11}$ system, and is largest in the $W_{89}Re_{11}$ systems.

Before He is inserted, the FWHM value is found largest for $W_{89}Ta_{11}$, and the values of W and $W_{89}Re_{11}$ are similar (Fig. S10(c)), indicating that the substitutional Ta atoms distorts the lattice the most significantly. The FWHM increases with He concentration for all the systems. The change rate of FWHM due to He concentration is smallest for the $W_{89}Ta_{11}$ system (Fig. S10(d)).

References

- [1] J. Das, A. Chakraborty, T. Bagchi, B. Sarma, Improvement of machinability

of tungsten by copper infiltration technique, *International Journal of Refractory Metals and Hard Materials* 26(6) (2008) 530-539.

[2] Y.-W. You, J. Sun, X. Wu, Y. Xu, T. Zhang, T. Hao, Q.F. Fang, C.S. Liu, Interplay of solute-mixed self-interstitial atoms and substitutional solutes with interstitial and substitutional helium atoms in tungsten-transition metal alloys, *Nuclear Fusion* 59(2) (2019) 026002.

[3] A. Jain, S.P. Ong, G. Hautier, W. Chen, W.D. Richards, S. Dacek, S. Cholia, D. Gunter, D. Skinner, G. Ceder, Commentary: The Materials Project: A materials genome approach to accelerating materials innovation, *APL materials* 1(1) (2013) 011002.

[4] X. Wu, X.-S. Kong, Y.-W. You, C.S. Liu, Q.F. Fang, J.-L. Chen, G.N. Luo, Z. Wang, Effects of alloying and transmutation impurities on stability and mobility of helium in tungsten under a fusion environment, *Nuclear Fusion* 53(7) (2013) 073049.

[5] L. Gharaee, P. Erhart, A first-principles investigation of interstitial defects in dilute tungsten alloys, *Journal of Nuclear Materials* 467 (2015) 448-456.

[6] S.-C. Lee, J.-H. Choi, J.G. Lee, Energetics of He and H atoms with vacancies in tungsten: First-principles approach, *Journal of Nuclear Materials* 383(3) (2009) 244-246.

[7] X.T. Zu, L. Yang, F. Gao, S.M. Peng, H.L. Heinisch, X.G. Long, R.J. Kurtz, Properties of helium defects in bcc and fcc metals investigated with density functional theory, *Physical Review B* 80(5) (2009).

[8] D. Lee, J.J. Vlassak, K. Zhao, First-Principles Theoretical Studies and Nanocalorimetry Experiments on Solid-State Alloying of Zr-B, *Nano Letters* 15(10) (2015) 6553-8.